

Ultrahigh Energy-Storage Density in NaNbO₃-Based Lead-Free Relaxor Antiferroelectric Ceramics with Nanoscale Domains

He Qi, Ruzhong Zuo,* Aiwèn Xie, Ao Tian, Jian Fu, Yi Zhang, and Shujun Zhang*

Dielectric energy-storage capacitors have received increasing attention in recent years due to the advantages of high voltage, high power density, and fast charge/discharge rates. Here, a new environment-friendly 0.76NaNbO₃–0.24(Bi_{0.5}Na_{0.5})TiO₃ relaxor antiferroelectric (AFE) bulk ceramic is studied, where local orthorhombic Pnma symmetry (R phase) and nanodomains are observed based on high-resolution transmission electron microscopy, selected area electron diffraction, and in/ex situ synchrotron X-ray diffraction. The orthorhombic AFE R phase and relaxor characteristics synergistically contribute to the record-high energy-storage density W_{rec} of $\approx 12.2 \text{ J cm}^{-3}$ and acceptable energy efficiency $\eta \approx 69\%$ at 68 kV mm^{-1} , showing great advantages over currently reported bulk dielectric ceramics. In comparison with normal AFEs, the existence of large random fields in the relaxor AFE matrix and intrinsically high breakdown strength of NaNbO₃-based compositions are thought to be responsible for the observed energy-storage performances. Together with the good thermal stability of W_{rec} ($>7.4 \text{ J cm}^{-3}$) and η ($>73\%$) values at 45 kV mm^{-1} up to temperature of $200 \text{ }^\circ\text{C}$, it is demonstrated that NaNbO₃-based relaxor AFE ceramics will be potential lead-free dielectric materials for next-generation pulsed power capacitor applications.

compared with other energy-storage devices due to the requirement of miniaturization and integration. The recoverable energy-storage density (W_{rec}) of dielectric capacitors can be determined from the area between the vertical axes and the polarization–electric field (P – E) discharge curve using the following formula

$$W_{\text{rec}} = \int_{P_r}^{P_{\text{max}}} E dP \quad (1)$$

$$W_{\text{loss}} = \int P dE \quad (2)$$

$$\eta = W_{\text{rec}} / (W_{\text{rec}} + W_{\text{loss}}) \quad (3)$$

where P_{max} is the saturated polarization, P_r is the remanent polarization, W_{loss} is the area of hysteresis loop, and η is the energy storage efficiency. It is clear that W_{rec} can be greatly enhanced with large polarization value at applied electric fields but with minimal remanent polarization. From this point of view, antiferroelectric (AFE) ceramics exhibit outstanding

advantages over other dielectrics as a result of the electric field-induced reversible AFE–ferroelectric (FE) phase transition.^[4–9]


Various types of AFE ceramics have been investigated in terms of their energy-storage characteristics, including lead-based and lead-free perovskite compounds, among which excellent W_{rec} values of 10.4, 7.02, and 4.4 J cm^{-3} have been reported in PbZrO₃ (PZ)-based,^[5] (Bi_{0.5}Na_{0.5})TiO₃ (BNT)-based,^[6] and AgNbO₃ (AN)-based^[7] AFEs, respectively. However, normal AFEs with macrodomains usually exhibit typical double P – E hysteresis loops with relatively low energy-storage efficiency because of the large hysteresis between the AFE–FE and FE–AFE phase transitions.^[8,9] That is to say, a large portion of the charged electric energy is dissipated as heat during discharging, as shown in **Figure 1a** (cyan part). In addition, extremely large phase switching current and large volume change are involved during loading/unloading, which tend to electrically and mechanically degrade the energy-storage performance.^[10] Generally, a slim hysteresis loop with low energy dissipation can be achieved by tailoring the domain size into micrometer (**Figure 1b**) or nanometer (**Figure 1c**) scales in either FEs or AFEs.^[6,11–17] The relaxor FEs with polar nano-regions exhibit hysteresis-free polarization response and

1. Introduction

Owing to the high power density and fast charge/discharge rates, dielectric capacitors have been the core component of numerous pulsed power systems.^[1–3] However, the energy-storage density of a capacitor needs to be significantly enhanced

Dr. H. Qi, Prof. R. Z. Zuo, Dr. A. W. Xie, Dr. A. Tian, Dr. J. Fu, Dr. Y. Zhang
Institute of Electro Ceramics and Devices
School of Materials Science and Engineering
Hefei University of Technology
Hefei 230009, P. R. China
E-mail: piezolab@hfut.edu.cn

Prof. S. J. Zhang
Institute for Superconducting and Electronic Materials
Australian Institute of Innovative Materials
University of Wollongong
NSW 2500, Australia
E-mail: shujun@uow.edu.au

 The ORCID identification number(s) for the author(s) of this article can be found under <https://doi.org/10.1002/adfm.201903877>.

DOI: 10.1002/adfm.201903877

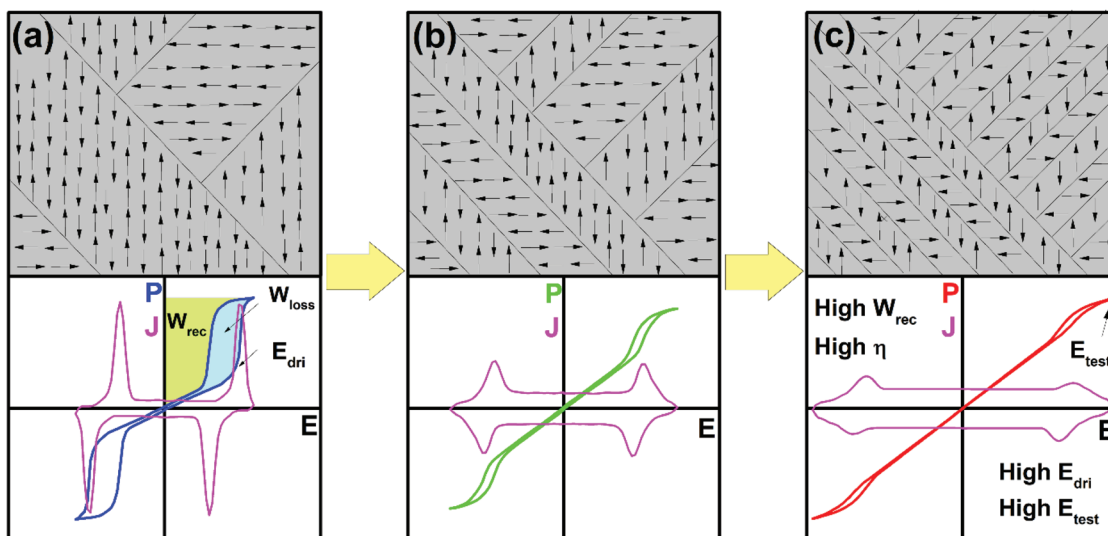


Figure 1. Schematic diagram of energy-storage properties for AFE ceramics with different domain morphologies: P - E loops and the corresponding polarization current density vs. electric field (J - E) curves for AFE ceramics with a) macrodomains, b) microdomains, and c) nanodomains.

require extremely high external electric field to construct a saturated long-range ordered FE state owing to the existence of local random fields.^[18] For the same reason, disruption of the long-range ordered AFE domains is expected to not only enhance the driving electric field (E_{dri}) for the AFE to FE phase transition owing to the weak interatomic interactions between the AFE nanodomain clusters, but also decrease the polarization hysteresis between loading and unloading owing to the fast response of nanoscale domains to the applied electric field (Figure 1c).^[18] Moreover, smaller phase switching currents associated with the smeared AFE-FE phase transitions would be in favor of the enhancement of the breakdown strength (E_{B}).

NaNbO_3 (NN) as a lead-free AFE material has recently received resurgent attention for energy-storage applications.^[19–27] However, its AFE P phase with a $Pbma$ space group is not stable at room temperature (RT) and tends to irreversibly transform to FE phase in response to a large external electric field. Many attempts have been focused on how to stabilize the AFE phase at RT by doping other ABO_3 perovskite phases or improving the fabrication process as the antiferroelectricity of NN depends on the grain size, density, and defects.^[20–22,28] Some NN-based solid solutions were reported to exhibit stable AFE orthorhombic P phase at RT, yet extremely large phase switching hysteresis was observed, in addition to their relatively low E_{B} and W_{rec} .^[24] Of importance is that improved W_{rec} can be attained in NN-based solid solutions with a relatively slim P - E loop at high applied electric fields;^[25–27] however, the structure-property relationship is yet unclear. In this work, the NN-BNT solid solution bulk ceramics were fabricated via a conventional high-temperature solid-state reaction method. The phase structure and domain morphology were explored by in/ex situ synchrotron X-ray diffraction (XRD), high-resolution transmission electron microscopy (HR-TEM), and the Rietveld structural refinement, while the energy-storage properties were evaluated based on field-dependent bipolar and unipolar P - E loops. Giant energy-storage density of

$W_{\text{rec}} \approx 12.2 \text{ J cm}^{-3}$ and satisfied efficiency $\eta \approx 69\%$ were obtained in 0.76NN–0.24BNT lead-free relaxor AFE ceramics with an orthorhombic $Pnma$ symmetry (R phase) and nanodomains with 30–50 nm in size.

2. Results and Discussion

2.1. Excellent Energy-Storage Properties

Figure 2a shows electric field-dependent P - E hysteresis loops at 10 Hz for the 0.76NN–0.24BNT ceramic. A nearly hysteresis-free linear P - E loop is observed at applied electric field below $E_{\text{dri}} \approx 36 \text{ kV mm}^{-1}$, corresponding to a polarization current density platform against applied field. The AFE nanodomains grow into microdomains and orient along the electric field direction over this electric field range, analogous to FE polar nanoregions responding to external fields.^[29] For a linear dielectric ceramic, W_{rec} can be given as follows

$$W_{\text{rec}} = \epsilon_0 \cdot \epsilon_r \cdot E^2 / 2 \quad (4)$$

According to Equation (4), a parabolic relationship between W_{rec} and E over field range of 0–30 kV mm^{-1} can be thus obtained and given in Figure 2b. The contribution from the orientation of AFE microdomains leads to the deviation from a parabolic relationship when the field is above 30 kV mm^{-1} but below E_{dri} , while the oriented AFE microdomains will gradually transform to long-range FE domains through phase transition as the applied electric field is over 36 kV mm^{-1} , leading to a nonlinear polarization response accompanied by an obviously hysteretic P - E loop. The obvious deviation from the parabolic relationship in the W_{rec} - E curve indicates that permittivity is sensitive to applied electric field above E_{dri} . A rapid decline η can be observed concurrently owing to the increased polarization hysteresis. Nevertheless, ultrahigh $W_{\text{rec}} \approx 12.2 \text{ J cm}^{-3}$ and

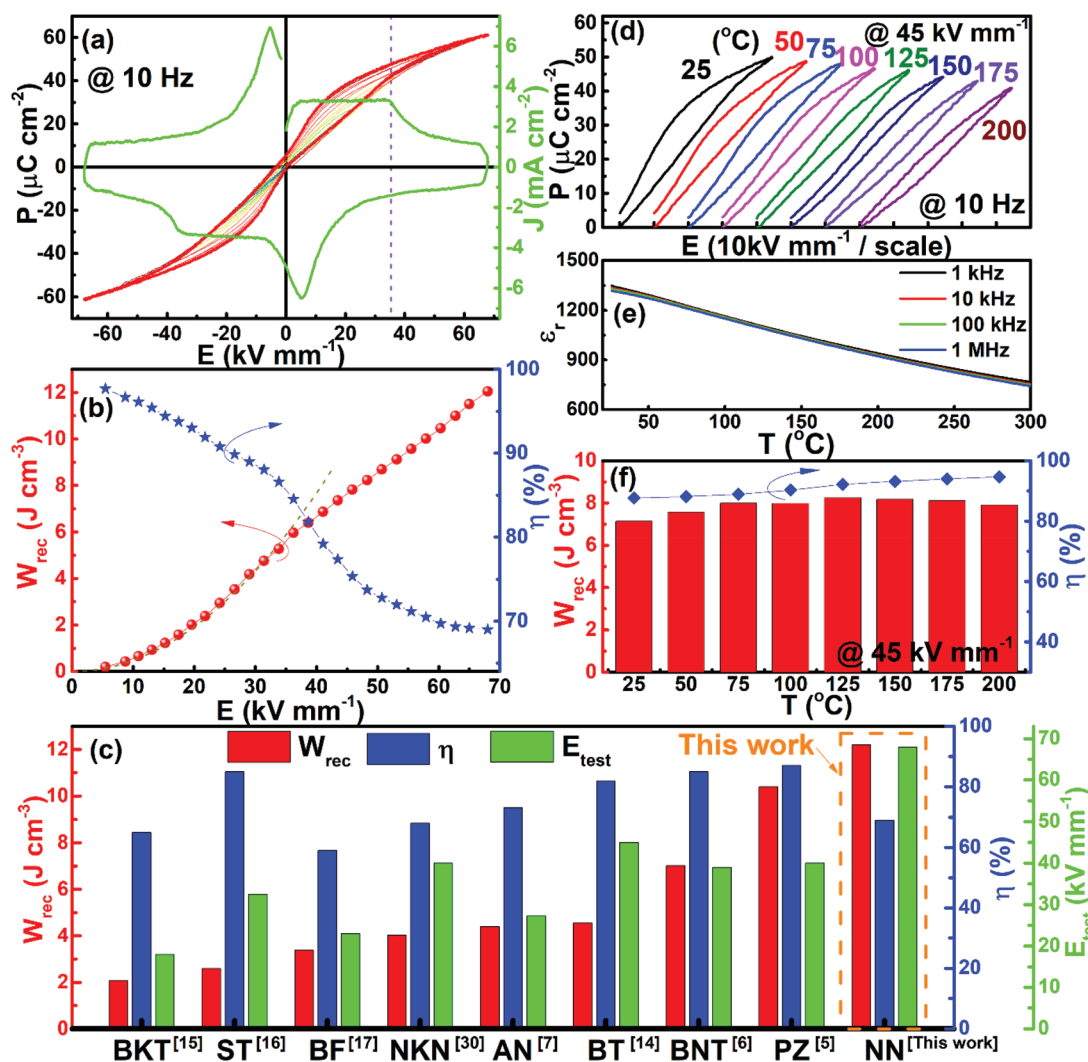


Figure 2. a) RT P - E loops under different electric fields and the corresponding J - E curves under 68 kV mm^{-1} for the 0.76NN-0.24BNT ceramic at a fixed frequency of 10 Hz; b) the variation of W_{rec} and η values of the 0.76NN-0.24BNT ceramic with the magnitude of the applied electric field; c) a comparison of W_{rec} , η , and test electric field values among the recently reported lead-containing and lead-free bulk ceramics with the maximum W_{rec} value of each system at RT; d) temperature-dependent P - E hysteresis loops; e) temperature- and frequency-dependent dielectric permittivity ϵ_r ; f) W_{rec} and η values as a function of measuring temperature for the 0.76NN-0.24BNT ceramic. BKT: $(\text{Bi}_{0.5}\text{K}_{0.5})\text{TiO}_3$, ST: SrTiO_3 , BF: BiFeO_3 , NKN: $(\text{Na}, \text{K})\text{NbO}_3$, BT: BaTiO_3 .

satisfied energy efficiency of $\eta \approx 69\%$ can be obtained simultaneously under an external electric field of $\approx 68 \text{ kV mm}^{-1}$ for samples with a thickness of 0.15 mm. The comparisons of the maximum W_{rec} values and corresponding η values, together with their test electric fields (E_{test}) for recently reported bulk dielectric ceramics, are given in Figure 2c.^[5-7,14-17,27,30] It can be clearly seen that the studied material in this research shows the highest $W_{\text{rec}} \approx 12.2 \text{ J cm}^{-3}$ in both lead-free and lead-based perovskite bulk ceramic systems. It should be noted that AFEs (NN, PZ, BNT, and AN) exhibit obvious advantages in energy-storage properties with large W_{rec} values against linear dielectrics and relaxor FEs. Of particular significance is that lead-free AFEs with nanodomains (NN- and BNT-based) possess large η values simultaneously, showing enormous potentials for high-power capacitor applications.

Figure 2d shows P - E loops of the 0.76NN-0.24BNT ceramic as a function of temperature under electric field of 45 kV mm^{-1} . Even though the achievable P_{max} value at 45 kV mm^{-1} decreases with increasing temperature owing to the reduced dielectric permittivity (see Figure 2e), a slight increase of η can be found (see Figure 2f) as the enhanced random field at elevated temperature helps increase the E_{dri} value. As a result, the W_{rec} value under 45 kV mm^{-1} slightly increases and then decreases on heating, with variation being on the order of +15% up to $200 \text{ }^\circ\text{C}$. A large W_{rec} of $>7.4 \text{ J cm}^{-3}$ as well as a desirable η of $>73\%$ can be obtained over the temperature range of RT- $200 \text{ }^\circ\text{C}$. It is clear that the studied material exhibits large potentials in the temperature stability of energy-storage properties against some other reported materials,^[6,7,9,31] such as BNT-based (3.5 - 3.8 J cm^{-3} in 25 - $250 \text{ }^\circ\text{C}$),^[6] AN-based

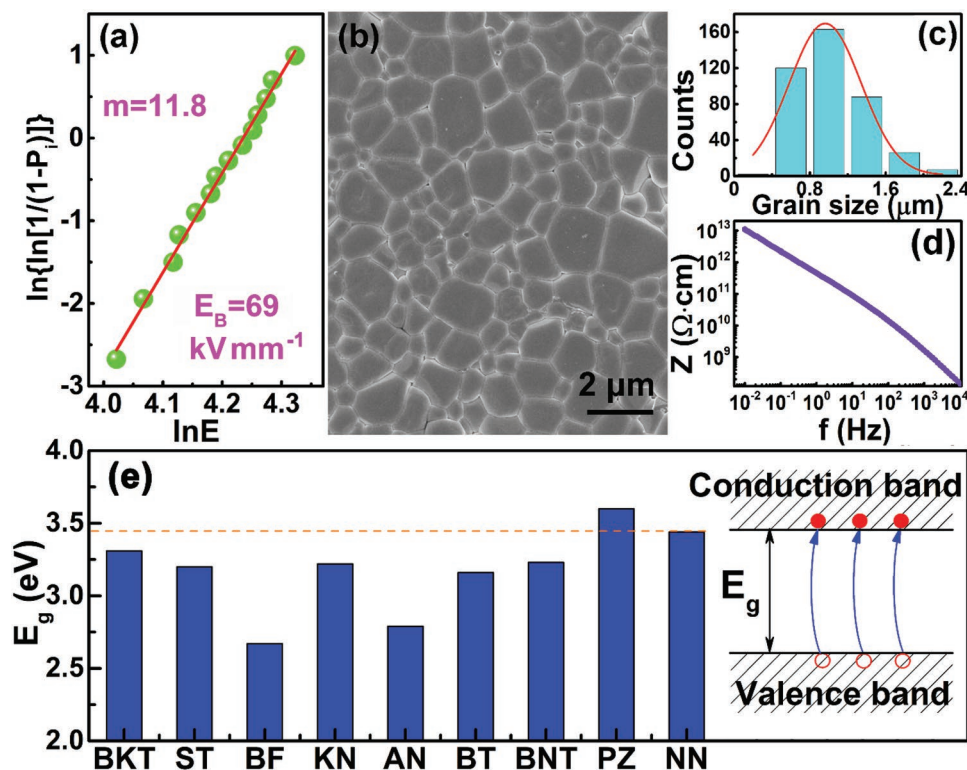


Figure 3. a) The Weibull distribution of the E_B , b) SEM image, and c) the corresponding histograms of the grain size distribution for the 0.76NN–0.24BNT ceramic; d) the variation of impedance (Z) with changing frequency; e) a comparison of the E_g value among various perovskites and a schematic illustration of electronic breakdown.

(4.4–4.5 J cm⁻³ in 20–120 °C),^[7] and Pb-based (4.9–5.6 J cm⁻³ in 30–90 °C)^[9] AFEs. The achieved good energy-storage performance is thought to be closely associated with the high E_B value and AFE domain morphology, which will be discussed in the following.

The value of dielectric breakdown strength E_B can be evaluated by using the Weibull distribution functions.^[32] As shown in **Figure 3a**, the data points fit well in the Weibull distribution with a slope of $m \approx 11.8$, demonstrating high reliability of the Weibull analysis. The higher shape parameter m indicates a smaller distribution range of the tested E_B values. To better understand such a high E_B value of ≈ 69 kV mm⁻¹ for the studied ceramic, the grain morphology is given in **Figure 3b**. Apart from a high relative density of $\approx 98\%$ with minimal porosity, uniform and fine grains with an average grain size of ≈ 1 μ m can be observed (see **Figure 3c**), which will benefit to enhanced breakdown strength. In addition, the RT impedance spectrum of the 0.76NN–0.24BNT ceramic is shown in **Figure 3d**, where a parallel resistor–capacitor equivalent circuit fitting result gives a large insulation resistance of over 5×10^{15} Ω cm, demonstrating a good insulation behavior. Furthermore, NN has a wider band gap (E_g), which is the forbidden energy gap between the top of the valence band and the bottom of the conduction band, than other lead-free ceramics,^[33–36] as shown in **Figure 3e**. For a narrow band gap, the electrons in the valence band are easy to jump into the conduction band, which would contribute to the conductivity as well as high possibility of intrinsic breakdown.^[3,33] Therefore, NN-based ceramics are

expected to have higher intrinsic E_B , as confirmed in **Figure 3a**, showing large advantages in energy-storage capacitors.

2.2. Nanodomains of Relaxor AFE

The bright-field TEM image of the lead-free AFE 0.76NN–0.24BNT ceramic is given in **Figure 4a**, exhibiting an irregular nanodomain morphology, which is consistent with the dielectric relaxation behavior observed in the insets of **Figure 4a**. Moreover, an increase of BNT substitution content is found to obviously enhance the dielectric relaxation degree, which accordingly increases the E_{dri} value of NN–BNT solid solutions. Such a high E_{dri} value for the AFE–FE phase transition in current work is thus believed to be associated with the existence of local random fields, owing to the enhanced compositional disorder induced by the substitution of BNT for NN, which can hinder the formation of long-range ordered domains. Irregular distribution of parallel stripes in grains can be observed along the $[100]_C$ direction, indicating the formation of nanodomains with 30–50 nm in size, as shown in **Figure 4b**. These nanodomains are obviously larger than the polar nanoregions (usually below 10 nm with a spherical shape) observed in ergodic relaxor FEs.^[37] To further reveal the hierarchical feature of domains, HR-TEM and selected area electron diffraction (SAED) patterns are shown in **Figure 4c–g**, revealing an ordered arrangement of atoms. The commensurate modulation stripes with a width ≈ 2.4 nm can be observed along the

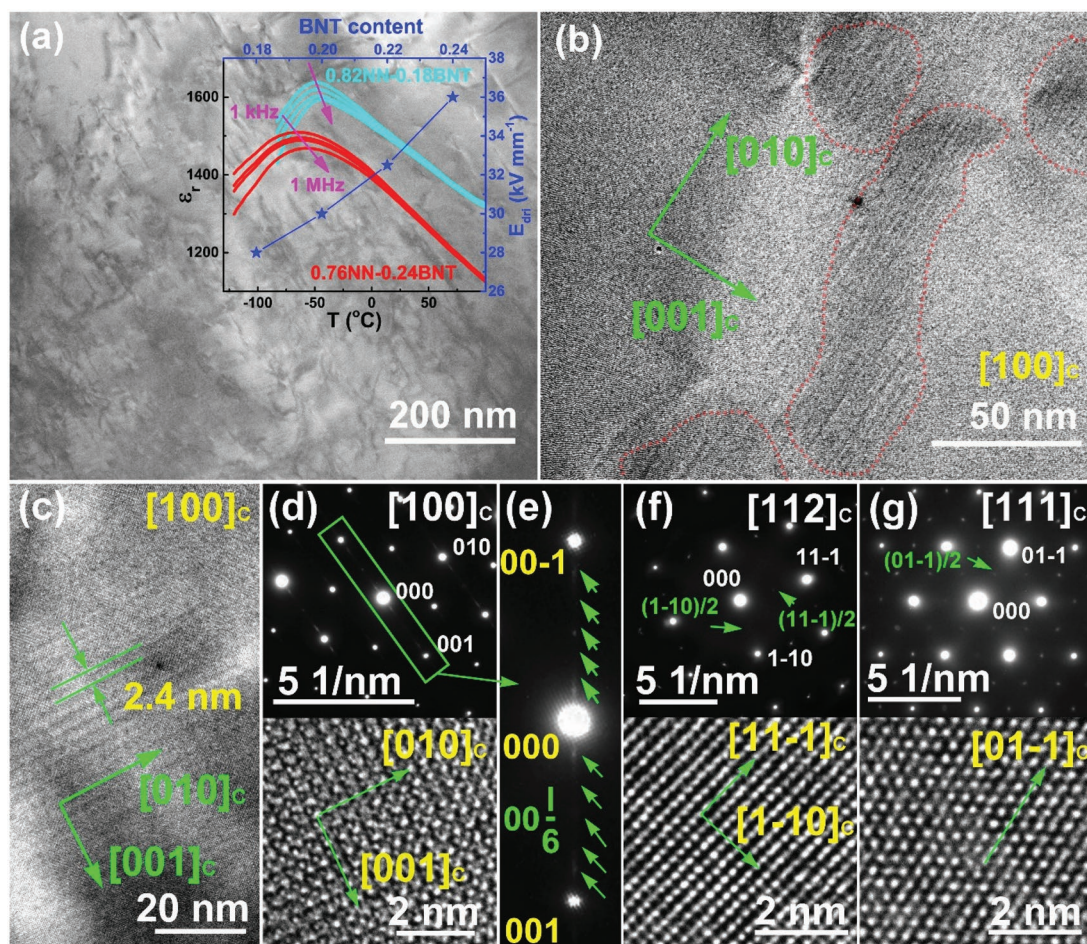


Figure 4. a–c) Domain morphologies on different scales, SAED patterns, and the HR-TEM images of lattice fringes along d,e) $[100]_c$, f) $[112]_c$, and g) $[111]_c$ for the 0.76NN–0.24BNT ceramic at RT. The insets of (a) show the temperature- and frequency-dependent dielectric permittivity ϵ' for the 0.76NN–0.24BNT and 0.82NN–0.18BNT ceramic and the evolution of E_{dri} with changing BNT content.

$[100]_c$ direction, which should correspond to the scale of AFE supercells along the c -axis, as shown in Figure 4c. It is reported that the formation of AFE phase is not only related to antiparallel off-center displacement of cations but also associated with octahedra tilting on the basis of a cubic structure, which can be described by Glazer notation,^[38] where the superscripts +, –, and 0 are used to explain whether successive octahedra along an axis have the same tilt, opposite tilt, and no tilt about that axis, respectively. Yet, Glazer notation is applicable to only $2 \times 2 \times 2$ supercell of the basic perovskite cell. For some AFE ceramics (e.g., $Pbma$ ($\sqrt{2} \times 4 \times \sqrt{2}$) and $Pnma$ ($2 \times 2 \times 6$) space groups) with longer periodic modulated phase, a new special notation that describes the tilts in terms of clockwise (C), anticlockwise (A), and zero (0) of adjacent octahedra was given by Peel et al.^[39] Based on this, the most possible structure model for the AFE orthorhombic R phase in NN is given as $Pnma$ with octahedral tilting system of $a^-b^+c^*$ ($c^* = A0CA0C$).^[39,40] Therefore, the existence of $(00l)/6$ superlattice in Figure 4e suggests that the local structure should be the AFE R phase with a $Pnma$ space group, revealing that the long periodic modulated AFE R phase has six basic perovskite cubic cells along the $[001]_c$ axis. Obvious superlattice can also be found in the

HR-TEM images of lattice fringes along $[100]_c$ in Figure 4d. Half superlattice reflections caused by the a^- and b^+ octahedral tilting can also be measured along the $[112]_c$ and $[111]_c$ directions, as shown in Figure 4f,g.

2.3. Evolution of Phase Structure under Electric Field

The AFE phase with $Pnma$ space group can also be identified by the Rietveld refinement of full XRD profiles measured at RT, as shown in Figure 5a. The reliability factors of weighted patterns (R_{wp}), patterns (R_p), and the goodness-of-fit indicator (χ^2) are 9.27%, 7.28%, and 1.68, respectively, indicating that the structural model is valid and the refinement result is reliable. The lattice parameter c of ≈ 23.35 Å is obtained, which is associated with the sixfold unit cell along the $[001]$ direction (see Figure 4c and the inset of Figure 5a). The $(100)_c$ and $(110)_c$ diffraction peaks under different fields were fitted by using PeakFit software with Pseudo-Voigt function, as shown in Figure 5b. Single $(100)_c$ and $(110)_c$ peaks with low intensity can be observed in the virgin sample, because AFE nanodomains are so small that their inherent orthorhombic symmetry can hardly

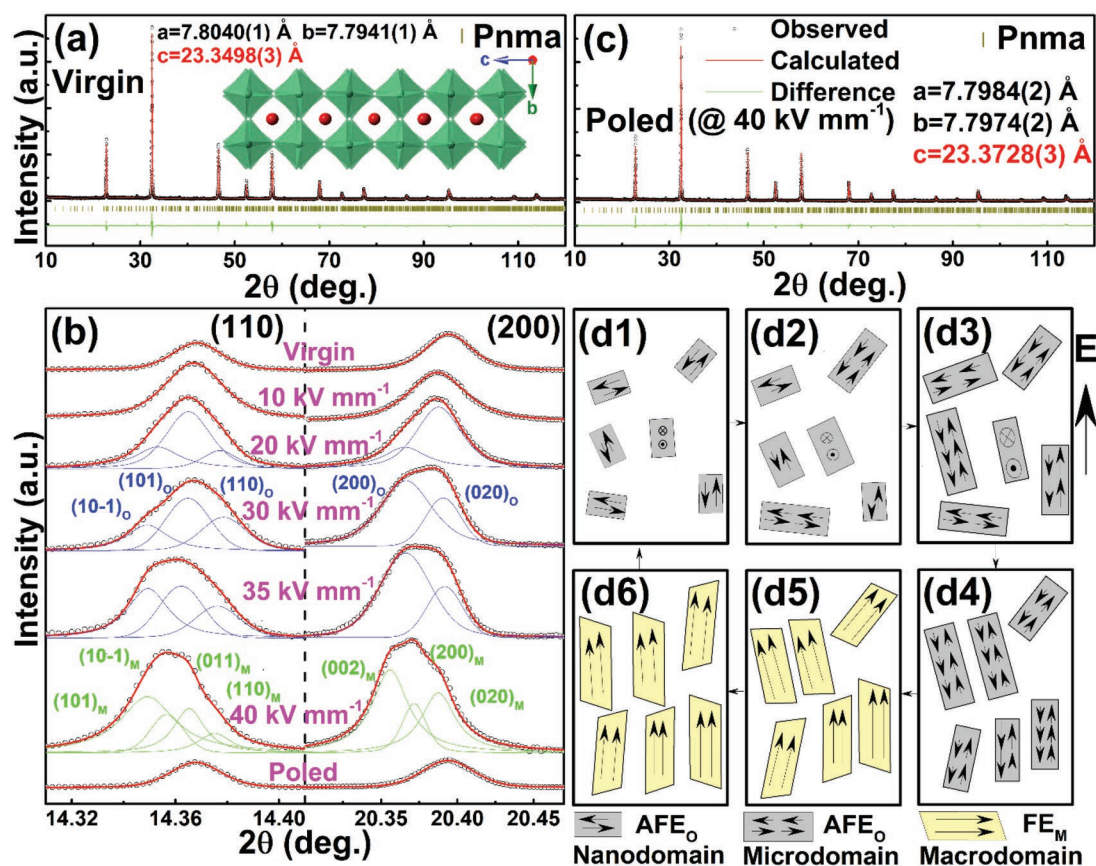


Figure 5. a) Rietveld structural refinement patterns of unpoled 0.76NN–0.24BNT ceramic powders; b) evolution of $(110)_C$ and $(200)_C$ reflections under various electric fields; c) Rietveld structural refinement patterns of poled ceramic powders for the 0.76NN–0.24BNT sample; d1–d6) schematic diagram of domain morphology and phase structure with changing the electric field. The inset of (a) is a view of the Pnma structure along the $[100]_C$ direction.

be resolved by X-ray diffraction.^[29] When an external field of 10 kV mm^{-1} is applied, an obviously enhanced peak intensity can be observed owing to the growth of nanodomains. With further increasing electric field, the $(110)_C$ triplet and $(200)_C$ doublet corresponding to its local orthorhombic symmetry can be detected starting at 20 kV mm^{-1} . The orthorhombic symmetry is clearly detected at 30 kV mm^{-1} , because the applied electric field is high enough to overcome the local random field related to the nanodomains. The growth of AFE nanodomains contributes to a linear polarization response, as shown in Figure 2a. With further increasing electric field up to 35 kV mm^{-1} , the AFE microdomains start to orientate along the electric field direction,^[10] as manifested by the obviously enhanced intensity of $(10-1)_C$ and $(200)_C$ peaks. At electric field of 40 kV mm^{-1} ($>E_{\text{dri}}$), a phase transformation from orthorhombic AFEs to monoclinic FEs occurs, as indicated by the additional reflections on both $(110)_C$ and $(200)_C$ peaks. The high-field FE macrodomains exhibit a certain orientation along the electric field, as observed by the relative intensity of the $(002)_M$ diffraction peak. The recovery of the weak $(110)_C$ and $(200)_C$ singlet peaks after removal of the external electric field further confirms that the field-induced AFE orthorhombic to FE monoclinic phase transition is completely reversible. The reversible AFE–FE phase transition can be further confirmed by means of the Rietveld structural refinement with a Pnma space group using the poled

ceramic powder sample, as shown in Figure 5c. The reliability factors of $R_{\text{wp}} = 9.09\%$, $R_p = 7.03\%$, and $\chi^2 = 1.43$ indicate that the poled 0.76NN–0.24BNT sample owns the same crystal symmetry as the virgin sample. The abovementioned transition process from initial AFE nanodomains to the long-range oriented FE macrodomains is schematically illustrated in Figure 5d. In comparison with the normal AFEs, the existence of large local random fields in relaxor AFE ceramics can effectively impede the growth of nanodomains and the subsequent phase transition process, which can assist the understanding of the mechanism responsible for the observed excellent energy-storage properties in the studied 0.76NN–0.24BNT AFE ceramics.

3. Conclusion

In summary, 0.76NN–0.24BNT lead-free relaxor AFE ceramics exhibit orthorhombic Pnma structure and typical nanoscale domains with 30–50 nm in size. The studied sample owns a stable antiferroelectric phase at RT and a reversible field-induced AFE–FE phase transition. Owing to the extremely large E_{dri} and E_B values, ultrahigh energy-storage density W_{rec} of $\approx 12.2 \text{ J cm}^{-3}$ and satisfied efficiency $\eta \approx 69\%$ can be simultaneously achieved in the studied AFE ceramic, showing great advantages over other bulk dielectric ceramics. The existence

of large random electric fields in the relaxor AFE matrix gives obstacle for the growth of AFE nanodomains and the subsequent AFE to FE phase transition, which leads to a nearly hysteresis-free polarization response at a high electric field up to 36 kV mm⁻¹. However, an electric field-driven AFE–FE phase transition accompanying a low-hysteresis domain orientation occurs during the second stage of higher fields (>36 kV mm⁻¹). Of particular significance is that desirable W_{rec} (>7.4 J cm⁻³) and η (>73%) values can be obtained over a wide temperature range up to 200 °C under 45 kV mm⁻¹, with variation being less than 15%. These results demonstrate that NN-based relaxor AFE R-phase ceramics would be a potential lead-free bulk dielectric material for next-generation pulsed power capacitor applications.

4. Experimental Section

Ceramic Fabrication: The (1 – x)NN–xBNT ceramic (0.18 ≤ x ≤ 0.24) was prepared by a conventional solid-state process using high-purity raw materials Na₂CO₃, Nb₂O₅, Bi₂O₃, and TiO₂ (AR, Sinopharm Chemical Reagent Co., Ltd., CN). The powders were weighed based on nominal composition and mixed in ethanol using zirconia balls for 12 h. The mixture was ball-milled again for 24 h after calcination at 900 °C for 5 h, then pressed into disk samples with a diameter of 10 mm under 100 MPa using polyvinyl alcohol as a binder. The disk samples were sintered at 1200–1350 °C for 2 h in air after burning out the binder at 550 °C for 4 h. The sintered sample discs were polished into a thickness of ≈0.15 mm, and then the two parallel surfaces were covered with silver paste and finally fired at 550 °C for 30 min as electrodes.

Ferroelectric Measurements: P–E loops at different temperatures were measured under a triangular field with a frequency of 10 Hz by using the ferroelectric testing system (Precision Multiferroic, Radiant Technologies Inc., Albuquerque, NM) connected to a high-temperature probing stage (HFS600E-PB2, Linkam Scientific Instruments, Tadworth, UK).

Dielectric Measurements: The dielectric permittivity as a function of temperature and frequency was measured by an LCR meter (Agilent E4980 A, Santa Clara, CA) at a heating rate of 180 °C h⁻¹.

Dielectric Breakdown Test: The E_B value was measured using a voltage breakdown tester (BDJC-50 kV, Beijing Beiguang Jingyi Instrument Equipment Co. Ltd, Beijing, China) on the sample with thickness of 0.15 mm and diameter of 3 mm. During the breakdown strength test, a dc voltage rising rate of 1 kV s⁻¹ was applied to each sample till the dielectric breakdown. The value of E_B was evaluated by using the following Weibull distribution functions^[32]

$$X_i = \ln(E_i) \quad (5)$$

$$Y_i = \ln\{\ln[1/(1-P_i)]\} \quad (6)$$

$$P_i = i/(n+1) \quad (7)$$

where n is the total number of the samples, E_i is the breakdown electric field for the i th specimen arranged in the ascending order, and P_i is the probability of dielectric breakdown.

SEM: The grain morphology was observed by using a field-emission scanning electron microscope (FE-SEM, SU8020, JEOL, Tokyo, Japan). Before the SEM observation, the samples were polished and thermally etched at ≈1000 °C for 30 min.

Impedance Measurements: The impedance as a function of frequency was measured by a broadband dielectric/impedance spectrometer (Concept 80, Novocontrol Inc., Germany).

TEM: The domain morphology observation, selected area electron diffraction, and high-resolution atomic imaging were performed on a field-emission transmission electron microscope (FE-TEM, JEM-2100F, JEOL, Japan) operated at 200 kV. For TEM examination, samples were first mechanically polished to a thickness of ≈20 μm and then ion-milled on a Precision Ion Polishing System (PIPS, Model 691, Gatan Inc., Pleasanton, CA, USA) at 5 kV. All specimens were annealed at 80 °C for at least one day to release the mechanical stress before the observation.

XRD: The phase structure was analyzed by a conventional powder X-ray diffractometer (D/Mzx-rB; Rigaku, Tokyo, Japan) with Cu K α radiation under an acceleration condition of 40 kV and 30 mA. The diffraction data were collected at steps of 0.01° of 2 θ over the range of 10–120°, at a scanning speed of 5° min⁻¹. The full XRD data were analyzed by the Rietveld refinement using GSAS software. Powders for the XRD measurement were prepared after gentle crushing of as-sintered and poled pellets in ethanol.^[41] Electric poling was carried out on the sintered pellets by applying a dc field of 40 kV mm⁻¹ for 5 min at RT.

In Situ Synchrotron XRD: Synchrotron XRD measurement was carried out on well-polished and Pt-sputtered disk samples under various electric field conditions at Shanghai Synchrotron Radiation Facility (SSRF) using beam line 14B1, which provided a monochromatic incident beam with a wavelength close to 0.6887 Å (18 keV). Measurements were performed by high-resolution θ –2 θ step-scans using a Huber 5021 six-circle diffractometer with a NaI scintillation detector.

Acknowledgements

This work was financially supported by National Natural Science Foundation of China (Grant No. 51472069) and China Postdoctoral Science Foundation (Grant No. 2018M642998). S.Z. gratefully acknowledges the support of ARC (FT140100698).

Conflict of Interest

The authors declare no conflict of interest.

Keywords

energy storage, lead free, NaNbO₃, nanodomains, relaxor antiferroelectric

Received: May 14, 2019

Revised: June 2, 2019

Published online:

- [1] B. J. Chu, X. Zhou, K. L. Ren, B. Neese, M. R. Lin, Q. Wang, F. Bauer, Q. M. Zhang, *Science* **2006**, 313, 334.
- [2] Z. H. Yao, Z. Song, H. Hao, Z. Y. Yu, M. H. Cao, S. J. Zhang, M. T. Lanagan, H. X. Liu, *Adv. Mater.* **2017**, 29, 1601727.
- [3] L. T. Yang, X. Kong, F. Li, H. Hao, Z. X. Cheng, H. X. Liu, J. F. Li, S. J. Zhang, *Prog. Mater. Sci.* **2019**, 102, 72.
- [4] A. Chauhan, S. Patel, R. Vaish, C. R. Bowen, *Materials* **2015**, 8, 8009.
- [5] H. S. Wang, Y. C. Liu, T. Q. Yang, S. J. Zhang, *Adv. Funct. Mater.* **2019**, 29, 1807321.
- [6] H. Qi, R. Z. Zuo, *J. Mater. Chem. A* **2019**, 7, 3971.
- [7] J. Gao, Y. C. Zhang, L. Zhao, K. Y. Lee, Q. Liu, A. Studer, M. Hinterstein, S. J. Zhang, J. F. Li, *J. Mater. Chem. A* **2019**, 7, 2225.
- [8] Y. Tian, L. Jin, H. F. Zhang, Z. Xu, X. Y. Wei, E. D. Politova, S. Y. Stefanovich, N. V. Tarakina, I. Abrahams, H. X. Yan, *J. Mater. Chem. A* **2016**, 4, 17279.

- [9] Q. F. Zhang, H. F. Tong, J. Chen, Y. M. Lu, T. Q. Yang, X. Yao, Y. B. He, *Appl. Phys. Lett.* **2016**, *109*, 262901.
- [10] S. E. Park, M. J. Pan, K. Markowski, S. Yoshikawa, L. E. Cross, *J. Appl. Phys.* **1997**, *82*, 1798.
- [11] H. R. Jo, C. S. Lynch, *J. Appl. Phys.* **2016**, *119*, 024104.
- [12] J. L. Li, F. Li, Z. Xu, S. J. Zhang, *Adv. Mater.* **2018**, *30*, 1802155.
- [13] G. Wang, J. L. Li, X. Zhang, Z. M. Fan, F. Yang, A. Feteira, D. Zhou, D. C. Sinclair, T. Ma, X. L. Tan, D. W. Wang, I. M. Reaney, *Energy Environ. Sci.* **2019**, *12*, 582.
- [14] W. Huang, Y. Chen, X. Li, G. S. Wang, N. T. Liu, S. Li, M. X. Zhou, X. L. Dong, *Appl. Phys. Lett.* **2018**, *113*, 203902.
- [15] F. Li, T. Jiang, J. W. Zhai, B. Shen, H. R. Zeng, *J. Mater. Chem. C* **2018**, *6*, 7976.
- [16] H. B. Yang, F. Yan, Y. Lin, T. Wang, *Appl. Phys. Lett.* **2017**, *111*, 253903.
- [17] H. G. Yang, H. Qi, R. Z. Zuo, *J. Eur. Ceram. Soc.* **2019**, *39*, 2673.
- [18] R. Z. Zuo, H. Qi, J. Fu, J. F. Li, M. Shi, Y. D. Xu, *Appl. Phys. Lett.* **2016**, *108*, 232904.
- [19] S. K. Mishra, N. Choudhury, S. L. Chaplot, P. S. R. Krishna, R. Mittal, *Phys. Rev. B* **2007**, *76*, 024110.
- [20] H. Shimizu, H. Z. Guo, S. E. Reyes-Lillo, Y. Mizuno, K. M. Rabec, C. A. Randall, *Dalton Trans.* **2015**, *44*, 10763.
- [21] H. Z. Guo, H. Shimizu, Y. Mizuno, C. A. Randall, *J. Appl. Phys.* **2015**, *117*, 214103.
- [22] L. M. Chao, Y. D. Hou, M. P. Zheng, M. K. Zhu, *Appl. Phys. Lett.* **2016**, *108*, 212902.
- [23] H. Z. Guo, H. Shimizu, C. A. Randall, *Appl. Phys. Lett.* **2015**, *107*, 112904.
- [24] Z. Y. Liu, J. S. Lu, Y. Q. Mao, P. R. Ren, H. Q. Fan, *J. Eur. Ceram. Soc.* **2018**, *38*, 4939.
- [25] M. X. Zhou, R. H. Liang, Z. Y. Zhou, S. G. Yan, X. L. Dong, *ACS Sustainable Chem. Eng.* **2018**, *6*, 12755.
- [26] Z. T. Yang, H. L. Du, L. Jin, Q. Y. Hu, S. B. Qu, Z. N. Yang, Y. Yu, X. Y. Wei, Z. Xu, *J. Eur. Ceram. Soc.* **2019**, *39*, 2899.
- [27] M. X. Zhou, R. H. Liang, Z. Y. Zhou, X. L. Dong, *J. Mater. Chem. A* **2018**, *6*, 17896.
- [28] L. M. Chao, Y. D. Hou, M. P. Zheng, Y. G. Yue, M. K. Zhu, *Appl. Phys. Lett.* **2017**, *110*, 122901.
- [29] W. L. Zhao, R. Z. Zuo, J. Fu, X. H. Wang, L. T. Li, H. Qi, D. G. Zheng, *J. Eur. Ceram. Soc.* **2016**, *36*, 2453.
- [30] T. Q. Shao, H. L. Du, H. Ma, S. B. Qu, J. Wang, J. F. Wang, X. Y. Wei, Z. Xu, *J. Mater. Chem. A* **2017**, *5*, 554.
- [31] W. X. Jia, Y. D. Hou, M. P. Zheng, Y. R. Xu, X. L. Yu, M. K. Zhu, K. Y. Yang, H. R. Cheng, S. Y. Sun, J. Xing, *J. Am. Ceram. Soc.* **2018**, *101*, 3468.
- [32] W. Weibull, *J. Appl. Mech.* **1951**, *18*, 293.
- [33] C. Kim, G. Pilania, R. Ramprasad, *J. Phys. Chem. C* **2016**, *120*, 14575.
- [34] G. Q. Li, T. Kako, D. F. Wang, Z. G. Zou, J. H. Ye, *J. Solid State Chem.* **2007**, *180*, 2845.
- [35] C. Pascual-Gonzalez, G. Schileo, S. Murakami, A. Khesro, D. W. Wang, I. M. Reaney, A. Feteira, *Appl. Phys. Lett.* **2017**, *110*, 172902.
- [36] H. Q. Sun, Q. W. Zhang, X. S. Wang, Y. Zhang, *Ceram. Int.* **2014**, *40*, 15669.
- [37] D. Fu, H. Taniguchi, M. Itoh, S. Mori, in *Advances in Ferroelectrics*, (Ed: A. Peláiz-Barranco), InTech, Rijeka, Croatia **2012**, pp. 51–67.
- [38] A. M. Glazer, *Acta Crystallogr., Sect. B: Struct. Crystallogr. Cryst. Chem.* **1972**, *28*, 3384.
- [39] M. D. Peel, S. P. Thompson, A. Daoud-Aladine, S. E. Ashbrook, P. Lightfoot, *Inorg. Chem.* **2012**, *51*, 6876.
- [40] S. K. Mishra, R. Mittal, V. Y. Pomjakushin, S. L. Chaplot, *Phys. Rev. B* **2011**, *83*, 134105.
- [41] D. K. Khatua, A. Senyshyn, R. Ranjan, *Phys. Rev. B* **2016**, *93*, 134106.